Science of the Total Environment 862 (2023) 161179

Contents lists available at ScienceDirect

Science of the Total Environment

journal homepage: www.elsevier.com/locate/scitotenv

The unaccounted dissolved iron (II) sink: Insights from dFe(II) concentrations in the deep Atlantic Ocean

David González-Santana [a,b,*], Alastair J.M. Lough [c], Hélène Planquette [a], Géraldine Sarthou [a], Alessandro Tagliabue [d], Maeve C. Lohan [c]

[a] Univ Brest, CNRS, IRD, Ifremer, LEMAR, F-29280 Plouzane, France
[b] Instituto de Oceanografía y Cambio Global, IOCAG, Universidad de Las Palmas de Gran Canaria, Las Palmas de Gran Canaria, Spain
[c] Ocean and Earth Science, University of Southampton, National Oceanography Centre, Southampton SO14 3ZH, United Kingdom
[d] Department of Earth Ocean and Ecological Sciences, School of Environmental Sciences, University of Liverpool, Liverpool, United Kingdom

HIGHLIGHTS

- Considering oxidation, open ocean iron (II) concentrations are below 0.2 nmol L^{-1}.
- The highest measured iron (II) concentration was 69.6 nmol L^{-1} at the Rainbow vent.
- In the open ocean iron (II) account for 20 % of the dissolved iron pool.
- Oxygen variations within OMZ account for 60 % of iron(II) oxidation variability.

GRAPHICAL ABSTRACT

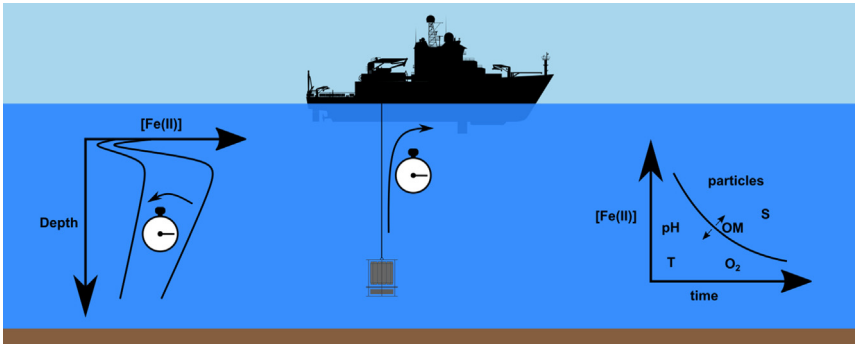

ARTICLE INFO

Editor: Julian Blasco

Keywords:
Iron oxidation
GEOTRACES
Hydrothermal
Biogeochemistry
Atlantic Ocean
(Min.5-Max. 8)

ABSTRACT

Hydrothermal vent sites found along mid-ocean ridges are sources of numerous reduced chemical species and trace elements. To establish dissolved iron (II) (dFe(II)) variability along the Mid Atlantic Ridge (between 39.5°N and 26°N), dFe(II) concentrations were measured above six hydrothermal vent sites, as well as at stations with no active hydrothermal activity. The dFe(II) concentrations ranged from 0.00 to 0.12 nmol L^{-1} (detection limit = 0.02 ± 0.02 nmol L^{-1}) in non-hydrothermally affected regions to values as high as 12.8 nmol L^{-1} within hydrothermal plumes. Iron (II) in seawater is oxidised over a period of minutes to hours, which is on average two times faster than the time required to collect the sample from the deep ocean and its analysis in the onboard laboratory. A multiparametric equation was used to estimate the original dFe(II) concentration in the deep ocean. The in-situ temperature, pH, salinity and delay between sample collection and its analysis were considered. The results showed that dFe(II) plays a more significant role in the iron pool than previously accounted for, constituting a fraction >20 % of the dissolved iron pool, in contrast to <10 % of the iron pool formerly reported. This discrepancy is caused by Fe(II) loss during sampling when between 35 and 90 % of the dFe(II) gets oxidised. In-situ dFe(II) concentrations are therefore significantly higher than values reported in sedimentary and hydrothermal settings where Fe is added to the ocean in its reduced form. Consequently, the high dynamism of dFe(II) in hydrothermal environments masks the magnitude of dFe(II) sourced within the deep ocean.

* Corresponding author at: Instituto de Oceanografía y Cambio Global, IOCAG, Universidad de Las Palmas de Gran Canaria, Las Palmas de Gran Canaria, Spain
E-mail address: david.gonzalez@fpct.ulpgc.es (D. González-Santana).

http://dx.doi.org/10.1016/j.scitotenv.2022.161179
Received 5 September 2022; Received in revised form 21 November 2022; Accepted 21 December 2022
Available online 26 December 2022

1. Introduction

Life developed before the Great Oxidation Event, approximately 2.4 billion years ago (Lyons et al., 2014), in an anoxic ocean, where anoxygenic photosynthesis with ferrous iron (Fe(II)) as the electron donor is thought to be the earliest type of photosynthetic process. The biological significance of iron (Fe) is based upon its past availability and its redox capabilities, with Fe(II) and ferric iron (Fe(III)) operating as electron acceptors or donors, respectively, for different dissimilatory processes (e.g. Straub et al., 2001, 2004). Therefore, due to Fe availability and its redox state at the origin of life, Fe(II) is still required in diverse metabolic pathways (Raven et al., 1999).

Today in oxic seawater the reduced Fe(II) is thermodynamically unstable and rapidly oxidises to its more stable redox state Fe(III) due to the presence of oxygen (O_2), superoxide ($O_2^{\bullet-}$) and hydrogen peroxide (H_2O_2) (Millero et al., 1987; Santana-Casiano et al., 2006). The chemical speciation of dFe in the ocean is dominated by dFe(III) (Bennett et al., 2008; Hawkes et al., 2013; Rue and Bruland, 1997). Iron (II) species have largely been considered to be "*picomolar concentrations of perhaps ephemeral species*" (Morel and Hering, 1993). Iron (II) is thought to be mainly in the soluble phase (Klar et al., 2017; Massoth et al., 1998; Millero et al., 1995; O'Sullivan et al., 1991) which oxidises rapidly. Iron (II) oxidation rates depend on the physical and chemical properties of seawater (primarily oxygen, pH and temperature), taking periods of minutes to hours to form iron oxyhydroxides with low solubility (Liu and Millero, 2002; Millero et al., 1987; Santana-Casiano et al., 2005). Iron (II) oxidation by oxygen can also be microbially mediated by lithotrophic bacteria such as *Zetaproteobacteria,* which are widely distributed in deep-sea environments forming biogenic Fe(III) minerals (Edwards et al., 2011; Emerson et al., 2007; Singer et al., 2011) or by nitrate (NO_3^-)-reducing Proteobacteria (Klueglein et al., 2014). All these processes blend to quickly reduce Fe(II) concentrations in the ocean.

Conversely, some processes increase the residence time of Fe(II). First, in the photic zone, most of the Fe(II) is produced by abiotic photoreduction of Fe(III) (Roy et al., 2008). Iron (III) reduction is not however limited to the photic zone, and can also occur via other abiotic processes. Abiotic reduction of Fe(III) with humic substances as electron shuttles has been previously shown (Voelker et al., 1997). This process occurs throughout the whole water column potentially fomenting the widespread distribution of Fe(II) in the deep ocean. Similarly, hydrogen sulphide (H_2S) can reduce Fe(III) oxyhydroxides (Yao and Millero, 1996). This is important in environments with high H_2S concentrations such as sulphide-rich hydrothermal environments. Moreover, numerous organisms can reduce Fe(III) using an array of electron donors (Maldonado and Price, 2001, 2000, 1999), including the microbial formation of superoxide which can reduce Fe(III) (Rose, 2012). Remineralization via microbial activity and grazing can reduce the Fe(III) bound to particulate organic matter acting as a source of Fe(II) (Boyd et al., 2010; Canfield et al., 2010; Moffett, 2021).

Hydrothermal vents are known to release significant quantities of Fe and sulfur minerals into the deep ocean with current estimates for Fe-release being on the order of 9×10^8 mol yr^{-1} (Tagliabue et al., 2010). Furthermore, these Fe-rich plumes can be transported for thousands of kilometres, having a broad basin-scale imprint on dFe distributions (Fitzsimmons et al., 2017, 2015; Nishioka et al., 2013; Resing et al., 2015; Sieber et al., 2021). Within hydrothermal plumes, the size fractionation of Fe species is modified and observations to date suggest Fe is found in three forms, nanoparticles, Fe-oxyhydroxides, adsorbed onto larger particles or associated with organic ligands (Bennett et al., 2008; Klar et al., 2017; Roy and Wells, 2011; Santana-González et al., 2019). The mechanisms by which hydrothermal Fe reaches the surface ocean and its impact on primary productivity are still an ongoing subject of debate within chemical oceanography research (Ardyna et al., 2019; Guieu et al., 2018; Roshan et al., 2020; Schine et al., 2021; Tagliabue and Resing, 2016). Iron in hydrothermal vent sites is sourced as Fe(II), which quickly oxidises to Fe(III) (González-Santana et al., 2021). Consequently, it is important to know the magnitude of iron that is sourced from ridge systems into the deep ocean.

In this manuscript, we report and discuss dissolved Fe(II) (dFe(II)) concentrations that were measured on samples collected during the 2017–2018 GEOTRACES GA13 section cruise following the Northern Mid-Atlantic Ridge, which intersects with the previous GA03w transect, a longitudinal transect across the Atlantic Ocean. The oxidation of Fe(II) to Fe(III) is the first reaction in a series of processes that dictate the transport of hydrothermal Fe through the ocean. To fully understand the importance of hydrothermal Fe in the ocean-climate system, we need an accurate picture of in-situ Fe(II) concentrations and how Fe(II) oxidation may differ between different vent sites. We focused on the distribution of Fe(II) concentrations through the Mid Atlantic Ridge (MAR) valley in the vicinity of six hydrothermal vents. We compared the dFe(II) concentrations to the dissolved Fe pool. Moreover, considering the time between sampling and analysis, we used a multiparametric equation to estimate the original Fe (II) concentration at the in-situ time of sampling. This dataset represents a substantial increase over the few studies which have reported Fe(II) distributions and includes samples from hydrothermal systems.

2. Materials and methods

2.1. Sampling sites

Sampling was performed along the MAR, during the GA13 UK GEOTRACES section that ran from Southampton (UK) to Guadeloupe (France) between December 2017 and February 2018, including six hydrothermal vent sites: Menez Gwen, Lucky Strike, Rainbow, Lost City, Broken Spur, and TAG. These six hydrothermal vent sites represent a wide range of geological conditions, which affect their hydrothermal properties. The location and main characteristics of these sites have been summarised in Table 1. A review of the geological characteristics of these sites was performed by Fouquet et al. (2013). Recently, the Fe(II) oxidation rate constants from these hydrothermal vent sites from samples collected during the same cruise were published by González-Santana et al. (2021).

The GA13 cruise can be divided into 4 components (Fig. 1). (1) A latitudinal transect, transect A, spanning 1900 km starting at the Menez Gwen hydrothermal site (37.842°N 31.521°W) and ending south of TAG (25.930°N 45.019°W). This transect crossed the six hydrothermal sites visited during the GA13 cruise along the MAR axis. (2) The longitudinal transect B was a 550 km section that covered the area north of the Azores. (3) Transect C was a 250 km transect intercepting the Rainbow vent site zonally. (4) Transect D was a 500 km long longitudinal transect crossing the TAG vent site zonally.

2.2. Sample collection

Thirty-two stations were sampled for dFe(II), dFe and pH. Seawater samples were collected according to the GEOTRACES guidelines (http://www.geotraces.org/images/Cookbook.pdf). Briefly, a titanium rosette fitted with 24 × 10 L trace metal-clean Teflon-coated OTE (Ocean Test Equipment) bottles, a CTD profiler (Sea-bird Scientific), and a redox potential sensor (PMEL MAPR), were deployed on a conducting Kevlar wire to collect samples from the water column. Sampling depths were chosen from the continuous temperature, salinity, and redox potential data.

To determine dFe(II) concentrations, a strict protocol was followed where samples were quickly collected and analysed once the rosette reaches the surface. Upon recovery, the OTE bottles were transported into an ISO Class 6 clean air van. Gases and short half-life species were subsampled first from the rosette. Dissolved Fe(II) samples were collected unfiltered into trace metal-clean 60 mL low-density polyethylene (LDPE) bottles without producing bubbles and without leaving any gas inside the bottles. González-Santana et al. (2021) shows that sample filtration in this step does not influence Fe(II) oxidation rates, so samples were not directly filtered and therefore, were collected at a faster rate. Samples were quickly inserted into an ice-filled cool box and samples were kept in the dark. Once these samples were collected, they were quickly transported to the trace metal clean analysis laboratory. The pH samples were collected in 125

Table 1
Location and main characteristics of the six studied hydrothermal vent sites. Table modified from Fouquet et al. (2013).

Name	Latitude	Longitude	Depth (m)	Basement Rocks	Geological Control	Distance from axis (km)	$[Fe]_{end\ member}$ (μM)
Menez Gwen	37°50′N	31°31′W	820	*E*-MORB	Top central volcano, axial graben, volcaniclastic	0	<2
Lucky Strike	37°17′N	32°16′W	1650	E-MORB	Top central volcano, lava lake (300 m), caldera	0	70–920
Rainbow	36°14′N	33°54′W	2400	Harzburgite	Center of nontransform offset, ultramafic dome	6	24,000
Lost City	30°10′N	42°10′W	700	Harzburgite	Top of an intersection massif, detachment fault	15	–
Broken Spur	29°10′N	43°10′W	3050	MORB	Top of neovolcanic ridge, axial summit fissure	0	1970
TAG	26°08′N	44°49′W	3670	MORB	Rift wall, central part of segment, volcanic centres	7	3830–5170

mL borosilicate bottles and kept in the dark until analysis. Samples for dFe were filtered through 0.45/0.2 μm two-step acetate membrane cartridge filters (Sartobran-300, Sartorius) into trace metal-clean 125 mL LDPE bottles and acidified to pH 1.7 (0.024 mol L^{-1}) by the addition of 12 mol L^{-1} ultrapure hydrochloric acid (HCl, Romil, UpA) under an ISO Class 6 laminar flow hood (Lohan et al., 2006). Samples for soluble Fe (sFe) went through an additional in-line filtration step inside a second laminar flow hood through 0.02 μm syringe filters (Anotop, Whatman) before acidification (Ussher et al., 2010).

2.3. Analytical methods

2.3.1. Dissolved iron (II) analysis

Dissolved Fe(II) was determined by flow injection analysis (FIA-CL) with in-line filtration through 0.2 μm syringe filters (Anotop, Whatman), preconcentration on resin-immobilised 8-hydroxyquinoline and chemiluminescence detection, modified after the method of Bowie et al. (2002). Sample flow rate was limited to below 1.5 mL min^{-1} to reduce possible cell lysis through the in-line filtration and to reduce the chance of filter breaking through the analysis. The in-line filter was exchanged between highly concentrated samples to reduce possible cross-contamination of samples. Due to low sampling volumes, changes in filters did not produce observable Fe(II) concentration changes. Luminol (Sigma-Aldrich) was cleaned using a Chelex 100 (Sigma-Aldrich) filled column. Standards used for shipboard analyses, including a primary stock solution of 0.02 mol L^{-1} dFe(II), were prepared weekly by dissolving ferrous ammonium sulphate hexahydrate (Fisher) in ultrapure 0.1 N hydrochloric acid solution (ROMIL); this solution was stabilised by the addition of 100 mmol L^{-1} sodium sulphite (Sigma-Aldrich). Working standards with concentrations of 200 mmol L^{-1} and 200 nmol L^{-1} dFe(II) were prepared daily by serial dilution of the primary stock solution with ultrapure 0.01 N and 0.001 N hydrochloric acid solution, respectively. Aged, low-Fe(II) seawater (obtained over 24 h before analysis from 2000 m depth and kept in the dark) adjusted to pH 5.5 with 2 mol L^{-1} ammonium acetate buffer was spiked with dFe(II) standard to obtain calibration standards generally in the range of 0–1 nmol L^{-1} dFe(II). For Fe-rich hydrothermal plume samples, preconcentration time was decreased and luminol concentration was halved to not overload the resin and keep the signal within the sensor detection range. For these samples, a second calibration was performed after the sample analysis with an increasing range until all the samples were encompassed. To eliminate Fe contamination after each hydrothermal station, the FIA-CL system was acid-cleaned, all the tubing was replaced and the system re-cleaned using 0.5, 0.1 nmol L^{-1} HCl and UHP water for 10, 30 and 60 min, respectively. Samples were analysed from deepest to the surface. The only exception was the first deployment at the Rainbow station (St. 16 cast 36), where due to the high turbidimeter signal, it was decided to start with the first sample above the hydrothermally affected water column. The sample at 2200 m was introduced into the FIA system but no concentration could be determined since the signal was above the detection window and the sample contaminated the preconcentration column and the analysis system. No other samples could be analysed in that cast. The system required the change of tubing and was acid cleaned during 48 h.

The analytical limit of detection was estimated daily as the dFe(II) concentration corresponding to a signal equal to three times the standard

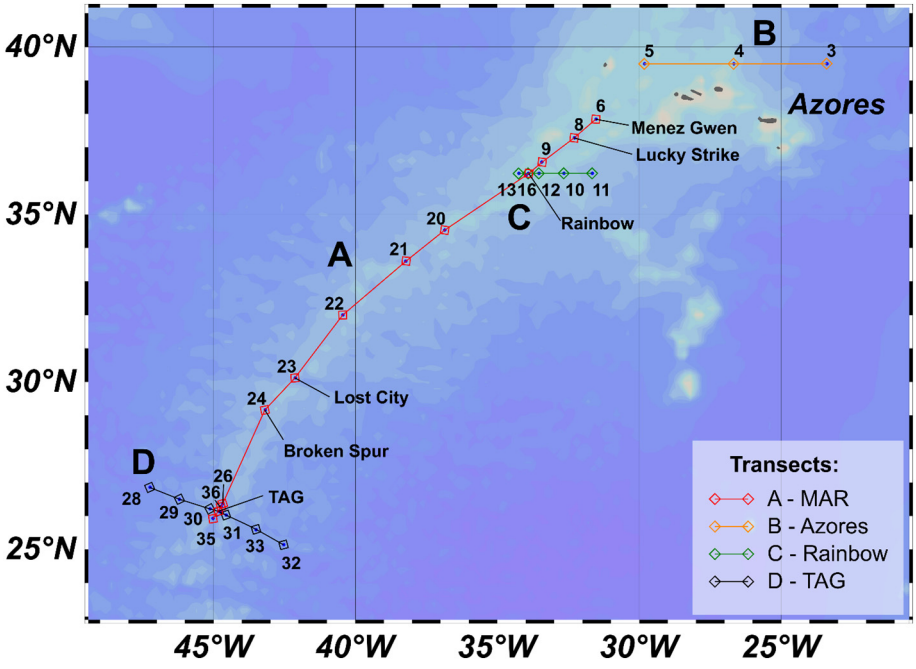

Fig. 1. Map showing the sampling stations for the GEOTRACES transect cruise GA13. The cruise track was divided into four transects (A (along the Mid Atlantic Ridge (MAR), red), B (north of the Azores, orange), C (across Rainbow, green) and D (across TAG, black)). Station numbers are shown; hydrothermal stations also include the vent site name.

deviation of quadruplicate analyses of the blank (Bowie et al., 2004; Sarthou et al., 2011). For the blank solution, we used filtered, aged, low-Fe(II) seawater that was stored in the dark for over 24 h. The average limit of detection was 0.02 ± 0.02 nmol L^{-1} (n = 42) for all the daily shipboard analyses. Currently, there are no Fe(II) intercalibration standards or reference materials that can be used to ascertain the accuracy of Fe(II) concentrations. We tried to mitigate this by preparing the primary Fe(II) stock weekly instead of monthly. This allowed for the intercomparison of two 0.2 nmol L^{-1} dFe(II) standards prepared from different primary stocks, with relative standard deviations of <10 %.

2.3.2. Dissolved and soluble iron analysis

Dissolved Fe was measured by flow injection chemiluminescence (Obata et al., 1993) at sea and soluble Fe (sFe) samples were analysed onshore. Measured values of 0.94 ± 0.04 for D2 reference material (n = 6) and 0.64 ± 0.03 for D1 (n = 6) were obtained by FIA-CL. High concentration dFe samples (>0.7 nmol L-1) were re-measured after 6 months of acidification by ICP-MS (Thermo Scientific, Element XR) using a standard addition method (Lough et al., 2019, 2017). GEOTRACES reference material D2 with 0.96 nmol L-1 Fe compared well with our measured values of 0.95 ± 0.06 nmol L-1 Fe (n = 6). In house standards with higher concentrations of Fe in the range of hydrothermal samples were measured repeatedly with relative standard deviations of 7 %. The complete dFe and sFe datasets will be reported in the next GEOTRACES data product.

2.3.3. pH analysis

The pH was potentiometrically measured on-board on the free scale using a Tris buffer solution (Millero, 1986). On-board pH samples were kept in the dark, inserted into a 25 °C water bath, and measured at this temperature, within less than 1 h after collection. The pH at in situ conditions were computed considering the total alkalinity for the average profile of the area (all available data between 15 and 50°N and 15–60°W; https://www.nodc.noaa.gov/ocads/oceans/GLODAPv2/, May 18th 2020) and the set of constants from Lueker et al. (2000). All the pH data are expressed in the free scale (data available in the supplementary material).

3. Results

3.1. Measured dissolved iron (II) concentrations

Measured dFe(II) concentrations throughout the water-column profile were low, with 90 % of the analysed samples (n = 362/403) having values below 0.2 nmol L^{-1}. Dissolved Fe(II) concentrations in non-hydrothermally affected stations remained relatively low through all the transects (Fig. 2). The maximum concentration was 0.12 nmol L^{-1} (n = 293). At shallow depths (< 500 m), dFe(II) concentrations were below 0.08 nmol L^{-1}, averaging 0.02 ± 0.02 nmol L-1 (n = 80). Higher dFe(II) concentrations were observed at deeper waters and within the top half of the bathypelagic zone (500 to 2000 m) averaging 0.07 ± 0.03 nmol L^{-1} (n = 108). Waters deeper than 2000 m presented lower concentrations averaging 0.05 ± 0.02 nmol L^{-1} (n = 105). Statistically significant ($P \leq 0.001$) differences were observed between the three depth sections when performing Wilcoxon Rank Sum Tests.

The FRidge cruise visited six hydrothermal vent sites. At these stations, due to the short distance from the hydrothermal vent, turbidity can be used as a good proxy of hydrothermal influence within the water column (González-Santana et al., 2020; Klinkhammer et al., 2001). Fig. 3 presents measured dFe(II) concentrations in the deep ocean close to the hydrothermal vent sites. Considering that dFe(II) oxidation rates can generally be theoretically determined as a function of temperature, pH, salinity and oxygen concentration (Santana-Casiano et al., 2005), Fig. 3 presents these variables.

At Menez Gwen (St. 6) the CTD data did not present any hydrothermal signal, presenting a nearly constant turbidity signal and a decrease in temperature (Fig. 3). The dFe(II) concentrations were similar to background values. Higher concentrations were observed in the bottom three samples (829–839 m). These samples were analysed consecutively and presented similar concentrations (0.24 ± 0.01 nmol L^{-1}). The pH values show similar behaviour, with the bottom three samples presenting a pH of 7.91.

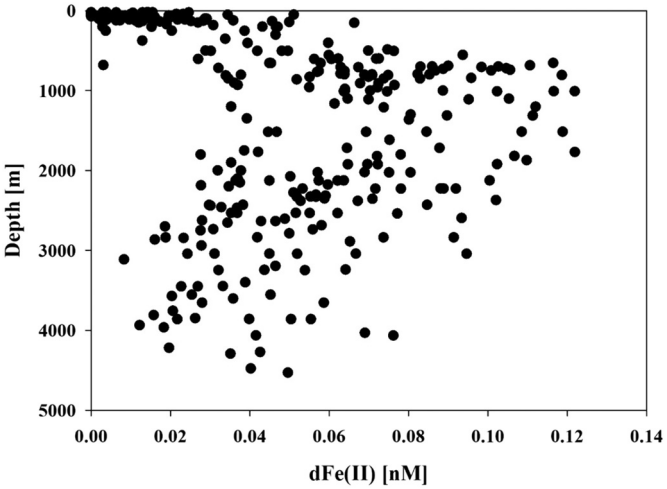

Fig. 2. Dissolved iron (II) concentrations in all non-hydrothermally affected stations (all stations except for 6, 8, 16, 23, 24, 35, 36) analysed during GEOTRACES cruise GA13.

At Lucky Strike (St. 8), cooler temperatures and higher oxygen concentrations were observed at depths deeper than 1600 m. These changes were opposite of what a hydrothermal signal should look like and are probably caused by a change in water mass. The four samples collected at depths deeper than 1670 m showed a strong dFe(II) source. The samples ranged from 0.47 to 0.77 nmol L^{-1} and were over 4 times background dFe(II) concentrations. This confirmed that the rosette was deployed close to an active vent site.

Dissolved Fe(II) was determined in two casts above the Rainbow vent site (St. 16 casts 36 and 43). During cast 36 a strong turbidity signal was observed between 1950 and 2170 m depth. This turbidity signal was 5 times higher than in Lucky Strike or Menez Gwen. The first analysed sample (2001 m) presented a dFe(II) concentration of 1.98 nmol L^{-1}. Concentrations increased within the hydrothermal plume. The sample located at 2108 m had a dFe(II) concentration above the calibration curve, reaching 12.8 nmol L^{-1}. No other samples could be analysed from this cast. The lowest pH was measured in the 2108 m sample reaching 7.87. The samples below this depth were slightly higher at pH 7.90. Cast 43 was deployed in the same location as cast 36. During this deployment, the turbidity signal was completely different. The plume observed during cast 36 had reduced to two smaller plumes centred at 1990 and 2025 m depth. On the other hand, a strong turbidity signal was observed at 2260 m. This maximum turbidity signal was higher than in the previous cast (0.60 and 0.48, respectively). This anomaly coincided with a temperature increase of 0.2 °C and an oxygen decrease of 1 μmol kg^{-1}. During this cast, dFe(II) measurements were focused on the maximum anomaly depths, where the highest dFe(II) was measured reaching 69.6 nmol L^{-1}.

Lost City (St. 23) is a low-temperature high pH sourced hydrothermal vent site. From previous research at this site, no high Fe source was expected. The dFe(II) concentrations were above the limit of detection and presented concentrations within the background level range, reaching a maximum of 0.11 nmol L^{-1}.

Brocken Spur (St. 24) presented a slight increase in turbidity at depths ranging from 2790 to 2900 m. The upper limit coincided with a rapid decrease in oxygen concentration of nearly 2 μmol kg^{-1} and a decrease in seawater temperature. The pH samples did not present much variability within these samples. However, dFe(II) concentrations increased significantly in samples from depths with higher turbidity, e.g. at the samples collected at 2829 and 2834 m depths with dFe(II) concentrations of 0.90 and 0.98 nmol L^{-1}, respectively.

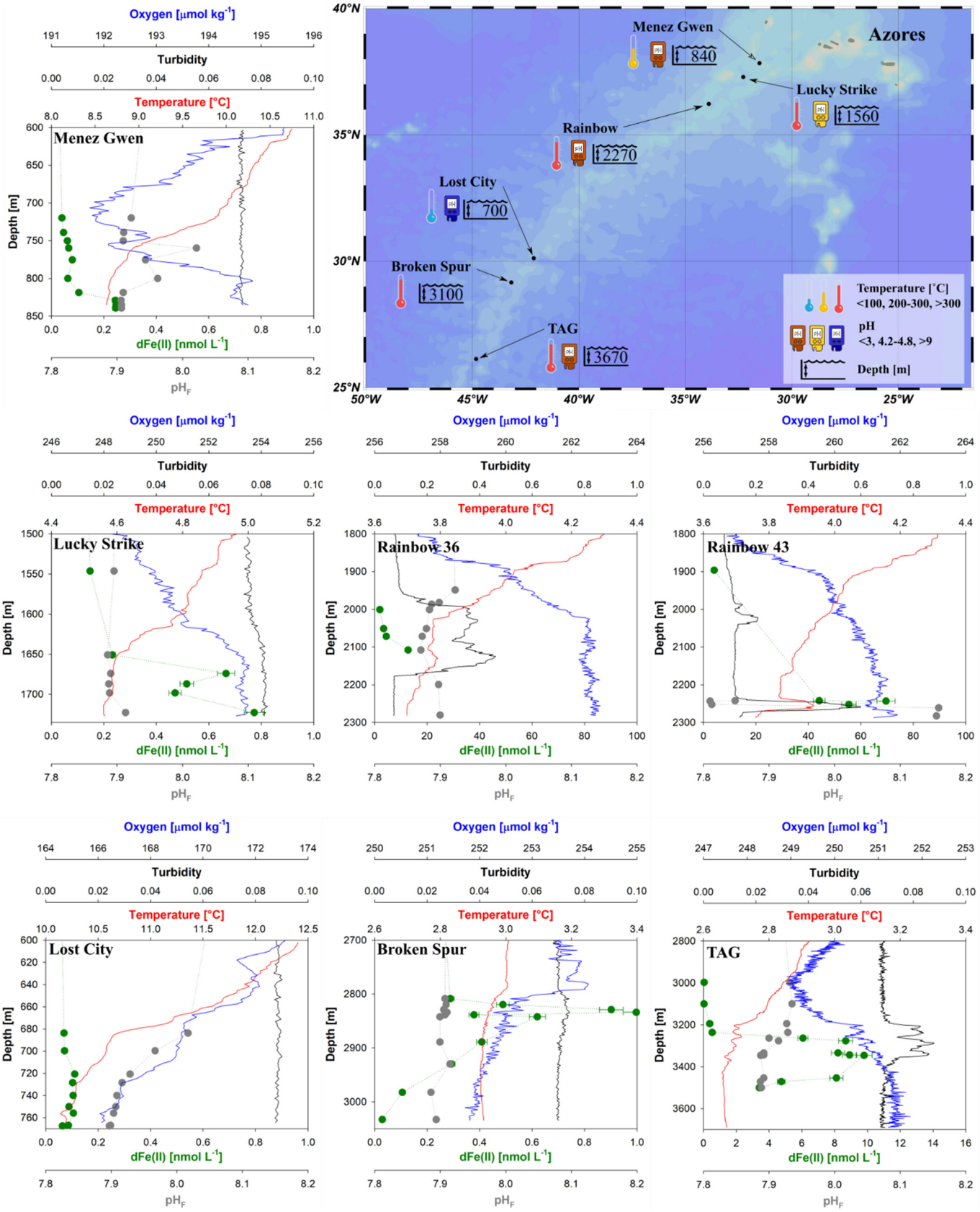

Fig. 3. Profiles at the six hydrothermal vent sites (two profiles at the Rainbow vent site). The map shows the location of each site along the MAR with a short summary of its characteristics: end member temperature, pH and depth. Each profile presents oxygen (blue), turbidity (black) and temperature (red) from the CTD and discrete measurements of dFe(II) concentrations (green) and pH_F (grey).

Above the TAG hydrothermal vent site, the hydrothermal activity could be identified using the turbidity signal. The rosette downcast and upcast presented a high turbidity signal between 3180 and 3360 m depth, with a decrease in turbidity at 3258 m. At the high turbidity depths, the temperature sensor presented a higher variability in the order of 0.02 °C. This hydrothermal signal occurred while changes in deep water masses caused oxygen concentrations to increase from 249 μmol kg^{-1} to 251 μmol kg^{-1} at depths >3000 m. The sample analysis showed that samples collected from the hydrothermally affected water column presented a decrease in pH. The pH varied from >7.93 above the high turbidity depth, to 7.92 in the top turbidity maximum and further decreased to 7.89 at depths >3258 m. Meanwhile, dFe(II) concentrations varied from background level (< 0.1 nmol L^{-1}) at depths shallower than 3200 m to concentrations as high as 9.8 nmol L^{-1}. Within the shallower turbidity maximum, dFe(II) concentrations remained high at 0.38 and 0.53 nmol L^{-1}. The higher dFe(II) concentrations were measured in the deeper plume section, where pH was lowest and averaged 7.89. The dFe(II) concentrations remained high even at the deepest sample (3500 m, 3.4 nmol L^{-1}) which was situated 150 m below the bottom of the deep turbidity maximum.

3.2. dFe(II) concentrations from a basin scale point of view

Hydrothermal sites act as strong focal sources of dFe(II) into the deep ocean. The dFe(II) profiles at all stations have been combined into vertical distribution diagrams of dFe(II) along the four FRidge transects (Fig. 4).

Along transect A, at Menez Gwen (St. 6), dFe(II) concentrations reached 0.25 ± 0.01 nmol L^{-1} at 829 m depth (15 m above the seafloor). Similarly, at Lucky Strike (St. 7), dFe(II) concentrations were high in the bottom 60 m (1674-1723 m), averaging 0.61 ± 0.14 nmol L^{-1} (n = 4). Station 9, a station not situated above a hydrothermal vent site, did not present any dFe(II) increases with concentrations in agreement with a non-hydrothermally affected station. At stations 20–23, including the alkaline vent Lost City, no dFe(II) anomalies were observed, with an average dFe(II) concentration of 0.05 ± 0.03 nmol L^{-1} (n = 78). At Broken Spur (St. 24), dFe(II) concentrations were >0.25 nmol L^{-1} below 2800 m (n = 8), reaching 0.95 ± 0.07 nmol L^{-1} (n = 2) at 2829 and 2834 m (~200 m above the seafloor).

Section B, a non-hydrothermal section above the Azores Plateau had dFe(II) concentrations with very low variability averaging 0.07 ± 0.03 nmol L^{-1} (n = 36). Transect C showed a very localised source, with a dFe(II) concentration averaging 6 ± 5 nmol L^{-1} (n = 4; between 1.98 and 12.8 nmol L^{-1}) at depths between 2000 and 2108 m (~160–270 m above the seafloor) at the Rainbow site (St. 16). At the four other stations of this transect, away from the Rainbow site, dFe(II) concentrations were similar to deep ocean background values (below 0.1 nmol L^{-1}) averaging 0.04 ± 0.03 nmol L^{-1} (n = 52).

From the seven stations (n = 137) of transect D across the TAG site, only the TAG system itself (St. 35) presented higher dFe(II) concentrations compared to background concentrations, averaging 8 ± 1 nmol L^{-1} (n = 6) in the neutrally buoyant plume depth (3263–3453 m). High concentrations below the plume 4.1 ± 0.9 nmol L^{-1} (n = 2) were also measured.

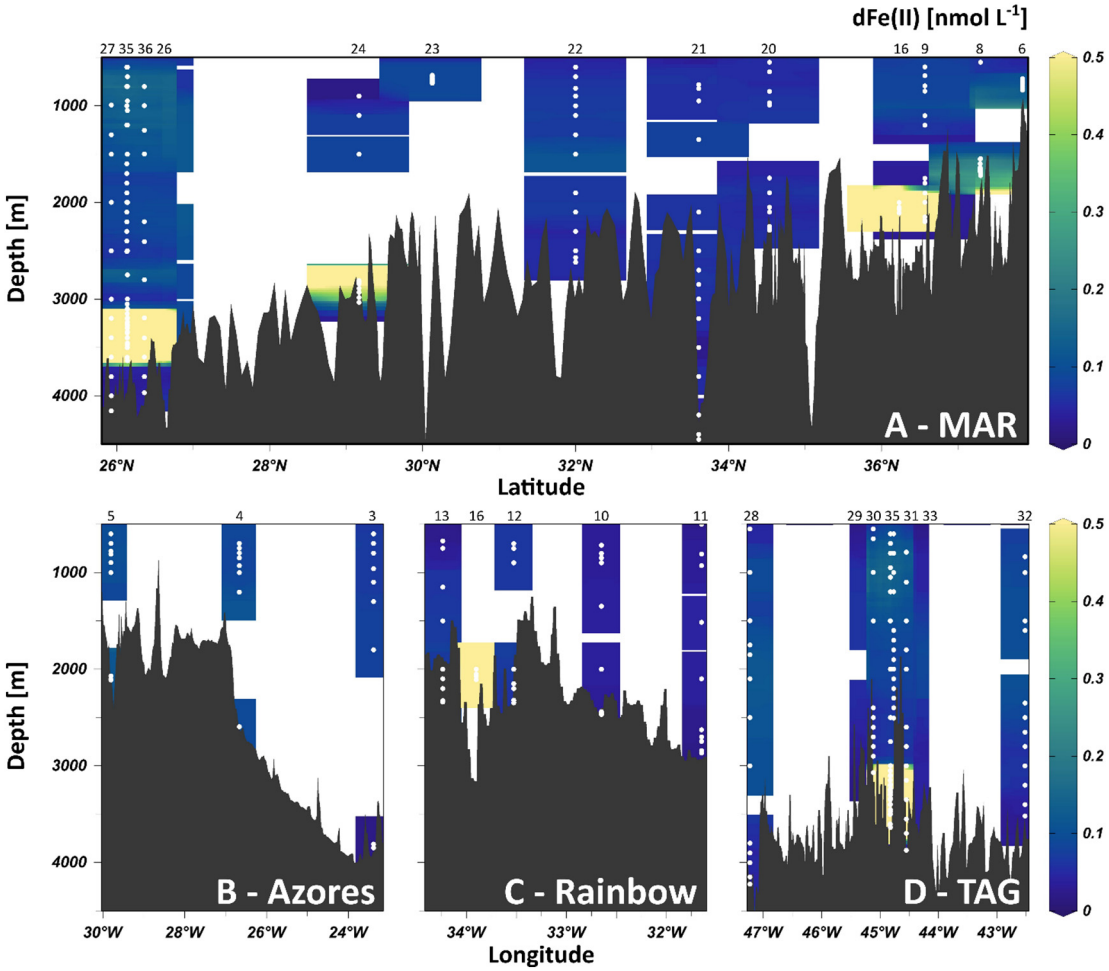

Fig. 4. Vertical sections of dFe(II) concentrations along the four transects of GEOTRACES cruise GA13 (refer to Fig. 1). Note that the maximum value of the colour scale is 0.5 nmol L^{-1}. Top x-axes present the station numbers. In A, stations 35 and 36 were located close to each other, so the label for station 26 has been displaced to the right. In D, stations between 29 and 33 were close to each other so the labels have been positioned relative to their spatial distribution of this data subset.

Moreover, at station 39 the ship was positioned at the same latitude and longitude as station 35, yet no hydrothermal dFe(II) signal could be observed in the deep samples, highlighting the variability in venting. Above TAG (St. 35, Fig. 4D), a regional maximum (0.22 ± 0.01 nmol L^{-1}, n = 4) was observed between 1000 and 1500 m depth, coinciding with the oxygen minimum zone.

To consider the effect of sampling and analyses time during this cruise on the measurements of dFe(II), an experiment was carried out with samples from the same depth collected into four 60 mL LDPE bottles. In this experiment, the first and second bottles were analysed consecutively (8 min between samples), while the third and fourth ones were analysed 24 and 48 min after the samples were collected. All these samples were maintained in the same conditions as all the other cruise samples (i.e., inside a dark ice-filled cool box). Results showed that the samples oxidised at a relatively consistent rate, which can be theoretically computed using the equation derived by González-Santana et al. (2021) (Supplementary Fig. 1). This short experiment demonstrated that dFe(II) oxidation was occurring within the LDPE bottles and was potentially also ongoing within the OTE bottles after samples were collected from the water column. This hypothesis agrees with the methodology used in Fe(II) oxidation kinetic experiments in hydrothermal vent sites during the '90s (Rudnicki and Elderfield, 1993), where the seawater was kept inside Niskin bottles and subsamples were collected at multiple time points.

3.3. Determining dissolved iron (II) concentrations post-sampling using oxidation rates

In oxygen saturated samples and a fixed pH, a pseudo-first-order rate dependence can be obtained to determine the rate at which Fe(II) oxidises (Eq. (1)). The k' is the pseudo-first-order rate constant which is strongly dependent on pH (Eq. (2)).

$$-d[Fe(II)]/dt = k'[Fe(II)] \quad (1)$$

$$k' = k[OH^-]^2[O_2] \quad (2)$$

The original dFe(II) concentration in the ocean ($dFe(II)_0$) can be related to the measured dFe(II) in the sample considering the elapsed time since sampling and the oxidation rate constant (k') (Eqs. (3)–(4)). The elapsed time since the bottles were closed was divided into four periods: *a*) from the timestamp on the CTD when the bottle fired to the transport of the OTE bottles inside the sampling van, *b*) sampling inside the clean lab van to the insertion of the subsample into the cool box, *c*) time required to collect other Fe(II) samples *d*) time spent in the laboratory inside the cool box before analysis. Time steps a-d were different for each sample and were all taken into account. We assume that the oxidation rate constants of steps *a* and *b* occurred at in situ temperature in a time $t_1 = t_a + t_b$, while steps *c* and *d* occurred at 2 °C (inside the cool box) in a time $t_2 = t_c + t_d$.

$$\ln\left[dFe(II)_{measured}\right] = \ln\left[dFe(II)_0\right] - k'\cdot t \quad (3)$$

$$\ln\left[dFe(II)_0\right] = \ln\left[dFe(II)_{measured}\right] + k'^{*}_{sal,(pH,T,O_2)_{in\ situ}}\cdot t_1 + k'^{*}_{sal,O_{2,in\ situ},(pH,T)_{2°C}}\cdot t_2 \quad (4)$$

The Fe(II) oxidation was considered to be well represented by a pseudo-first-order rate constant, k' (Eqs. (1) and (2)) computed using the updated multiparametric equation from the same samples in this work (Eq. (5); González-Santana et al., 2021).

$$\log k'(s^{-1}) = 35.627 - 6.7109{*}pH + 0.5342{*}pH^2 - 5434.02/T - 0.04406{*}S^{1/2} - 0.002847{*}S \quad (5)$$

The computed k' values in Eq. (5) were determined at saturated oxygen concentrations. To consider the effect of the oxygen concentration variability in the Fe(II) oxidation, the oxidation rate constant k (non-oxygen dependent) was calculated from Eq. (2). A new k' (k'^{*}) for the in-situ oxygen concentration was then calculated reapplying Eq. (2) using the obtained k and the in situ O_2 concentration. For non-hydrothermally affected samples, the experimental data and the theoretically derived data presented a standard error of estimate in log k' of ±0.2287 (k' in min^{-1}), which corresponds to a half-life error of less than 1 min. The multiparametric equation is temperature, pH, salinity and oxygen-dependent (Supplementary Fig. 2). We assumed constant oxygen concentration in the transport of the samples, as we minimised air exchange during sampling and salinity. Eq. (3) was modified to compute the original in situ concentrations ($dFe(II)_0$) considering the two oxidation rate constants (Eq. (4)). These equations do not include biological interactions, such as organic matter, which depending on its composition can accelerate or retard the oxidation rate constant (Santana-Casiano et al., 2000; Theis and Singer, 1974). Generally, the organic matter effect in samples within the first 500–800 m can produce slower oxidation rates than theoretically determined using Eq. (5), so this section of the profile has not been included. Similar to previous dFe(II) work, hereafter, measured dFe(II) concentrations will be reported as dFe(II), while calculated dFe(II) concentrations will be defined as $dFe(II)_0$.

3.3.1. Impact of oxidation on dissolved iron (II) concentrations

The $dFe(II)_0$ concentrations were computed for oceanic profiles between 500 and 4500 m depth (Fig. 5). Above 500 m, where Fe(II) oxidation $t_{1/2}$ are only a few minutes, the extrapolation of the $dFe(II)_0$ could not be determined with the existing equation. Similarly, Fe(II) oxidation rate constants determined with the theoretical equation are severely underestimated within hydrothermal plumes. This phenomenon was explained in González-Santana et al. (2021). As such, measured Fe(II) $t_{1/2}$ in Rainbow were as low as 17.3 min when the calculated Fe(II) $t_{1/2}$ was 39 ± 3 min. This variation in $t_{1/2}$ would produce an underestimation of $dFe(II)_0$ within the hydrothermal plumes.

The average dFe(II) concentration in non-hydrothermally affected seawater below 500 m depth was 0.06 ± 0.03 nmol L^{-1} (Fig. 4). The calculated $dFe(II)_0$ in those same samples increased to 0.25 ± 0.14 nmol L^{-1} (Fig. 5). The resulting measured dFe(II) concentrations averaged 28 ± 9 % of $dFe(II)_0$. The smallest differences between dFe(II) and $dFe(II)_0$ corresponded to deep ocean samples with seawater temperatures below 4 °C (e.g. St. 20, T = 3.5 °C) or samples collected at shallow casts within the maximum remineralization depth (e.g. St. 4, at 700–1000 m depth the O_2 was <210 μmol kg^{-1}).

3.3.2. Relationship between dFe(II) with dFe and sFe

The $dFe(II)_0$ concentrations were compared to the dFe concentrations (dFe = dFe(II) + dFe(III)). On average 23 ± 16 % of the dFe pool was $dFe(II)_0$ in non-hydrothermally affected seawater below 500 m depth (Fig. 6). This percentage was influenced by the samples collected at the 500–800 m depth. Samples deeper than 800 m presented $dFe(II)_0$/dFe ratios of 17 ± 10 %. In deep samples close to hydrothermal vent sites, measured dFe(II) concentrations increased. The measured dFe(II) concentration at Rainbow (St. 16, 2108 m) was 12.8 nmol L^{-1}, and corresponded to 54 % of the dFe pool. These high percentages were also measured at Broken Spur (St. 24, 2930 m, dFe(II) = 0.29 nmol L^{-1}, dFe(II)/dFe = 31 %) and TAG (St. 35, 3334–3454 m, dFe(II) = 8.2–9.8 nmol L^{-1}, dFe(II)/dFe = 27–43 %).

In hydrothermal environments, sFe decreases within the buoyant plume while colloidal iron increases (Lough et al., 2019). The size fractionation is affected by the oxidation of Fe(II). The Fe(II) which initially should be mainly in the soluble phase, would oxidize forming iron-bearing silicates, iron-oxyhydroxides and iron-manganese oxides (Humphris et al., 2015) increasing the Fe found in larger size fractions (colloidal and particulate). The dFe samples are collected after the unfiltered samples and after mixing and pressurizing all the OTE bottles. During this sampling time, Fe(II) within the OTE bottles should have oxidised (Supplementary Fig. 1) decreasing the available sFe(II); which would increase cFe and pFe concentrations. Similarly, sFe samples are collected from dFe samples which are filtered offline. This filtration time would cause sFe(II) to oxidize potentially forming cFe. Consequently, oxidation in environments with high Fe(II)

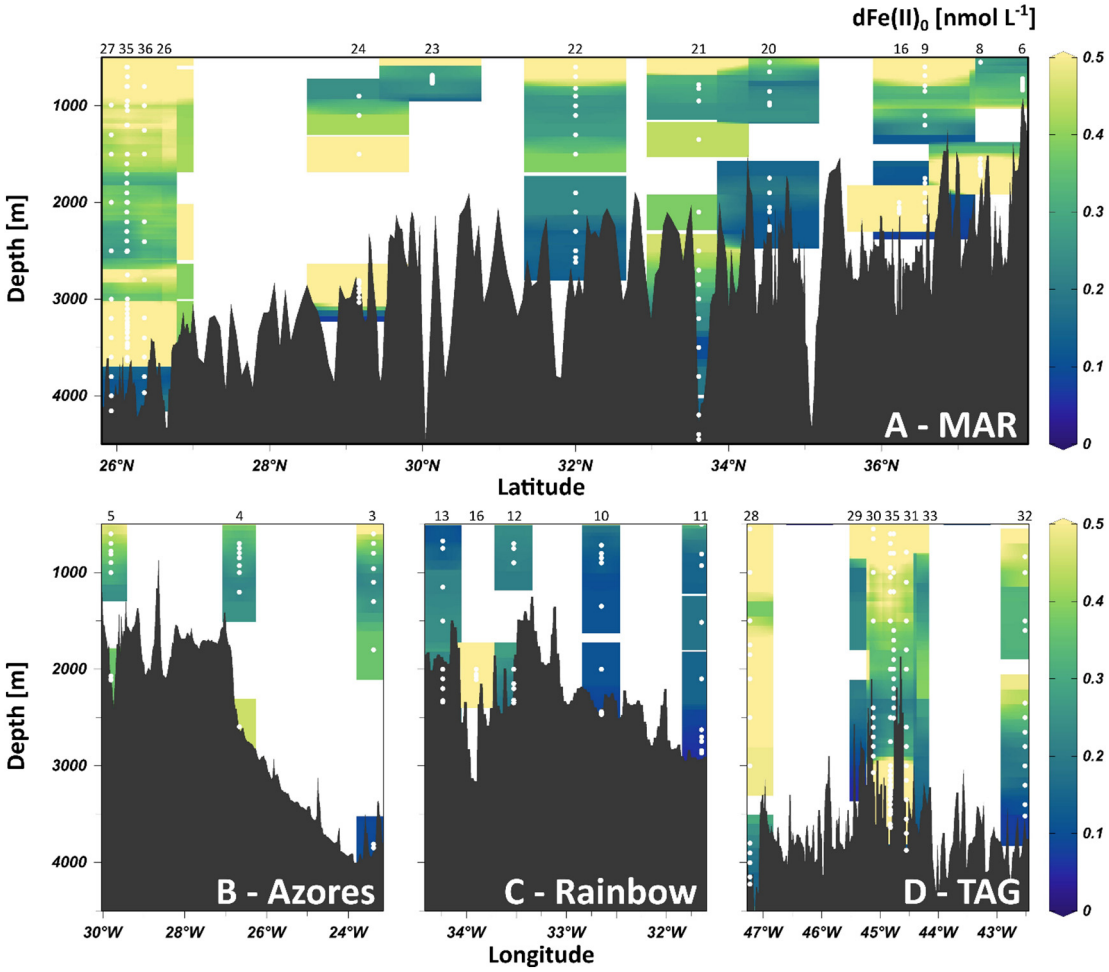

Fig. 5. Vertical sections of dFe(II)$_0$ concentrations along the four transects of GEOTRACES cruise GA13 (refer to Fig. 1). Note that the top 500 m of the profile have not been included (see text for detail). The maximum value of the colour scale is 0.5 nmol L^{-1}. Top x-axes present the station numbers. In A, stations 35 and 36 were located close to each other, so the label for station 26 has been displaced to the right. In D, stations between 29 and 33 were close to each other so the labels have been positioned relative to their spatial distribution of this data subset.

could affect the dFe(II)/dFe and dFe(II)/sFe ratios (and similarly with dFe(II)$_0$). This phenomenon was observed when calculating dFe(II)$_0$/dFe ratios close to three hydrothermal vent sites, Rainbow (St. 16, 2108 m), Broken Spur (St. 24, 2930 m) and TAG (St. 35, 3334–3454 m). In these three stations dFe(II)/dFe ratios were 54, 31, 27–43 % respectively and ascended to 116, 108 and 112–140 % when we calculated the dFe(II)$_0$/dFe.

The dFe(II)$_0$ concentrations were also compared to the sFe concentration (Fig. 7). The dFe(II)$_0$ concentrations were generally below sFe concentrations. Samples in non-hydrothermally affected seawater below 500 m depth presented dFe(II)$_0$ concentrations averaging 24 ± 16 % sFe concentrations (Fig. 7). The exceptions were observed within hydrothermal plumes, where dFe(II) was above the sFe concentrations. When the dFe(II)$_0$/sFe percentages were calculated at stations 21 and 23, many samples collected between 500 and 2000 m (e.g. Fig. 7B and C) presented percentages close to averaging 100 or below. However, close to the vent sites, percentages above 200 % were obtained at Menez Gwen (210 %, St. 6), Lucky Strike (210 %, St. 8), Rainbow (>700 %, St. 16), Broken Spur (210 %, St. 24) and TAG (>1000 %, St. 35).

4. Discussion

Figs. 2 and 4 show the spatial and depth ubiquity of dFe(II) throughout the transects, with above limit of detection concentrations in all the samples. Previous work performed at depths deeper than 1000 m were characterised by low dFe(II) concentrations with many samples presenting concentrations close to the analytical limit of detection. As such, work performed in the Eastern North Atlantic presented dFe(II) concentrations below or close to 0.1 nmol L^{-1} (Boye et al., 2006). These concentrations agree with our dFe(II) measurements averaging 0.06 ± 0.03 nmol L^{-1} in the non-hydrothermally affected waters. Boye et al. (2006) measured dFe(II) concentrations of up to 0.55 nmol L^{-1} towards the East of the Azores. In Section B, across the North of the Azores, we did not find concentrations above 0.14 nmol L^{-1}. In the Atlantic sector of the Southern Ocean, labile Fe(II) concentrations reached up to 0.05 nmol L^{-1} at depths below 2100 m (Sarthou et al., 2011), being within our measured dFe(II) range in the North Atlantic. More recently, samples collected in the North Atlantic Ocean during the GA03 showed dFe(II) concentration below 0.2 nmol L^{-1} except for the station above the TAG hydrothermal vent site (Sedwick et al., 2015).

The tendency of Fe(II) is to oxidize rapidly in seawater, with a $t_{1/2}$ that can vary from minutes to hours in a medium rich in oxygen depending on the conditions of pH and T (Santana-Casiano et al., 2005). The uncertainty that arises in oceanographic studies is whether the measured dFe(II) represents all the dFe(II) initially present in the water column or if there are losses during sampling due to oxidation. Limited basin-scale dFe(II) transect data have been reported to date, largely due to the difficulties involved in measuring dFe(II). Hansard et al. (2009) revealed the first values through two CLIVAR transects across the Pacific Ocean (PO2 and P16N). The second basin-scale report was performed by Sedwick et al. (2015) across the U.S. GEOTRACES GA03 transect. Similarly, a study for labile Fe(II) (Fe(II) in

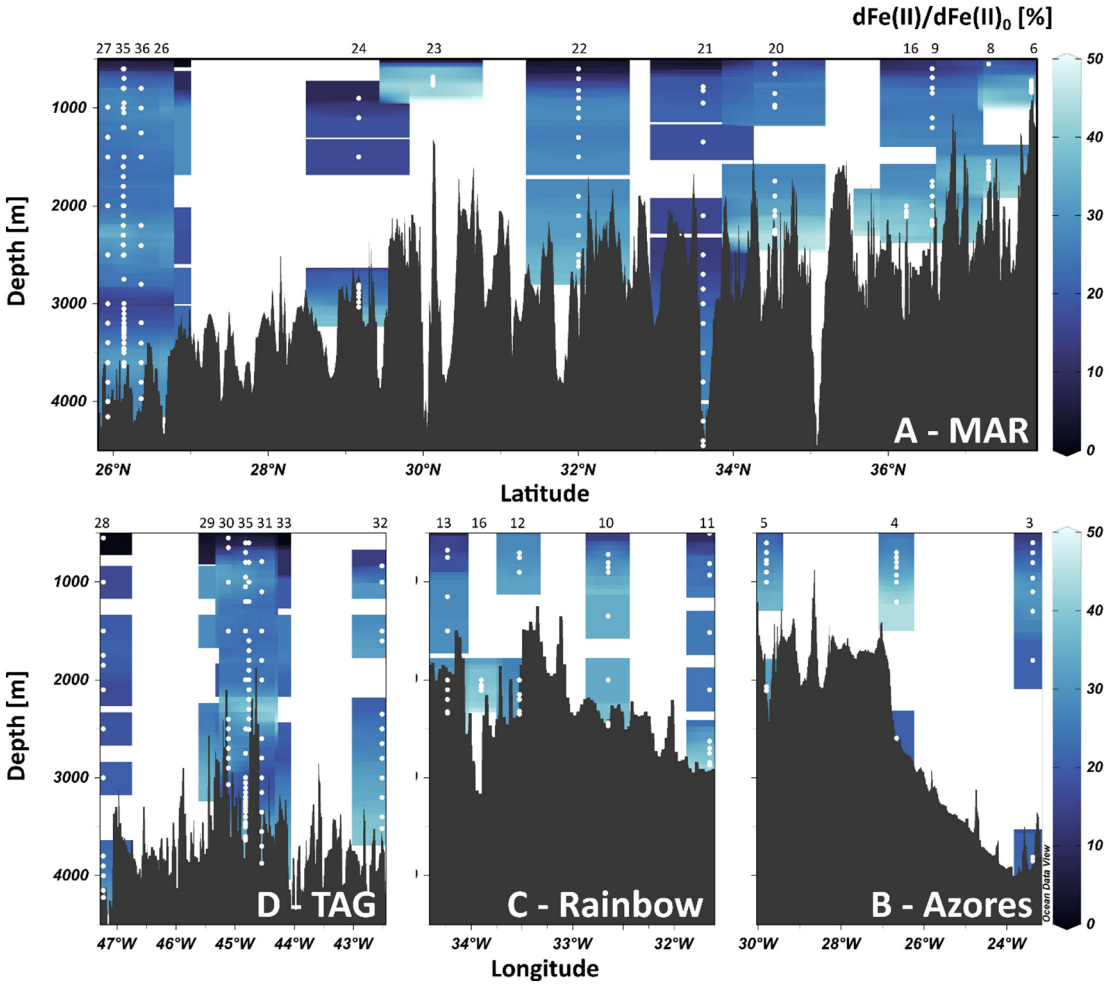

Fig. 6. Vertical sections of the measured dFe(II) as a percentage of dFe(II)$_0$ (dFe(II)/dFe(II)$_0$ [%]) concentration along the four transects of GEOTRACES cruise GA13 (refer to Fig. 1). Note that the top 500 m of the profile have not been included. The maximum value of the colour scale is 50 %. Top x-axes present the station numbers. In A, stations 35 and 36 were located close to each other, so the label for station 26 has been displaced to the right. In D, stations between 29 and 33 were close to each other so the labels have been positioned relative to their spatial distribution of this data subset.

unfiltered samples) and Fe(II) oxidation, was reported by Sarthou et al. (2011). Iron(II) has also received interest in shallow process studies and oceanic regions (eg. Schallenberg et al., 2015; Vedamati et al., 2014).

In this work, we have considered that the Fe(II) oxidation process is dynamic and that it is conditioned, at all times, by the environmental conditions, as temperature changes. This has led us to analyse the possible changes experienced by the oxidation rate constant of Fe(II) from the time the sample is collected until it is analysed. This will allow for future comparisons of dFe(II) concentrations between different ocean basins/environments.

4.1. Iron (II) in the water column

Figs. 2–4 present measured dFe(II) concentrations within the North Atlantic Ocean. However, dFe(II) is lost to oxidation during the ascent of the rosette, during the subsampling interval, and during the analysis interval (Supplementary Fig. 1). To mitigate this effect, the dFe(II)$_0$ was calculated (Fig. 5). The average $t_{1/2}$ time for all samples was 27 ± 17 min (maximum of 58 min) for in situ oxygen, temperature and pH conditions and increased to 40 ± 15 min (maximum of 67 min) for the samples within the cool box (2 °C). When considering that the rosette ascends at a rate of 1 m s^{-1} (1–3 m min^{-1} when triggering the bottles), a rosette that ascends 3600 m will take at least 1 h to reach the surface without considering sampling and analysis time. As a result, the idea of a sample that has suffered 1 to 2 Fe(II) oxidation $t_{1/2}$ should be considered when reporting Fe(II) concentrations.

The dFe(II)$_0$ values indicate that even though deep samples were the first to be collected, the cold temperatures counterbalanced the oxidation of the Fe(II). As a result, samples collected from depths deeper than 1000 m may have maintained 20 to 45 % of their initial Fe(II) concentrations even for deepest samples collected at depths beyond 4000 m. Similarly, shallower stations such as 4, 5, 10, 12 and 13 were the least affected due to the limited ocean depth and hence the sampling time was the shortest.

In seawater Fe(II) is mainly found in the soluble phase as Fe^{2+} (75.8 %), $FeOH^+$ (1.0 %) and $FeHCO3^+$ (0.5 %) (Millero et al., 1995). Iron (II) is also found in the colloidal size fraction as $FeCO_3^0$ (22.6 %). In hydrothermal environments, the presence of dissolved sulphide allows for the formation of nano pyrite (FeS), with sizes in the colloidal size fraction range (Findlay et al., 2019). Consequently, the presence of cFe(II) will affect the dFe(II)/sFe and dFe(II)$_0$/sFe ratios in hydrothermal environments, as observed in the high percentages of dFe(II)$_0$/sFe in Fig. 7. This is an effect of the formation of cFe(II) nanoparticles (e.g. nano-pyrite). However, the high dFe(II)$_0$/dFe percentages at Rainbow (St. 16, 2108 m, 116 %), Broken Spur (St. 24, 2930 m, 108 %) and TAG (St. 35, 3334–3454 m, 112–140 %) describe a sampling bias related to the oxidation of Fe(II), where it is aggregating forming larger size particles.

The dFe(II)$_0$ concentrations were generally below dFe concentrations, representing 17 ± 10 % of the deep ocean (>800 m) dFe pool. The relevance of dFe(II)$_0$ increased to 23 ± 16 % of the dFe pool when the 500–800 m depth samples were also included. This increase in the relative fraction of dFe(II) in the dFe pool was previously observed by Sarthou et al.

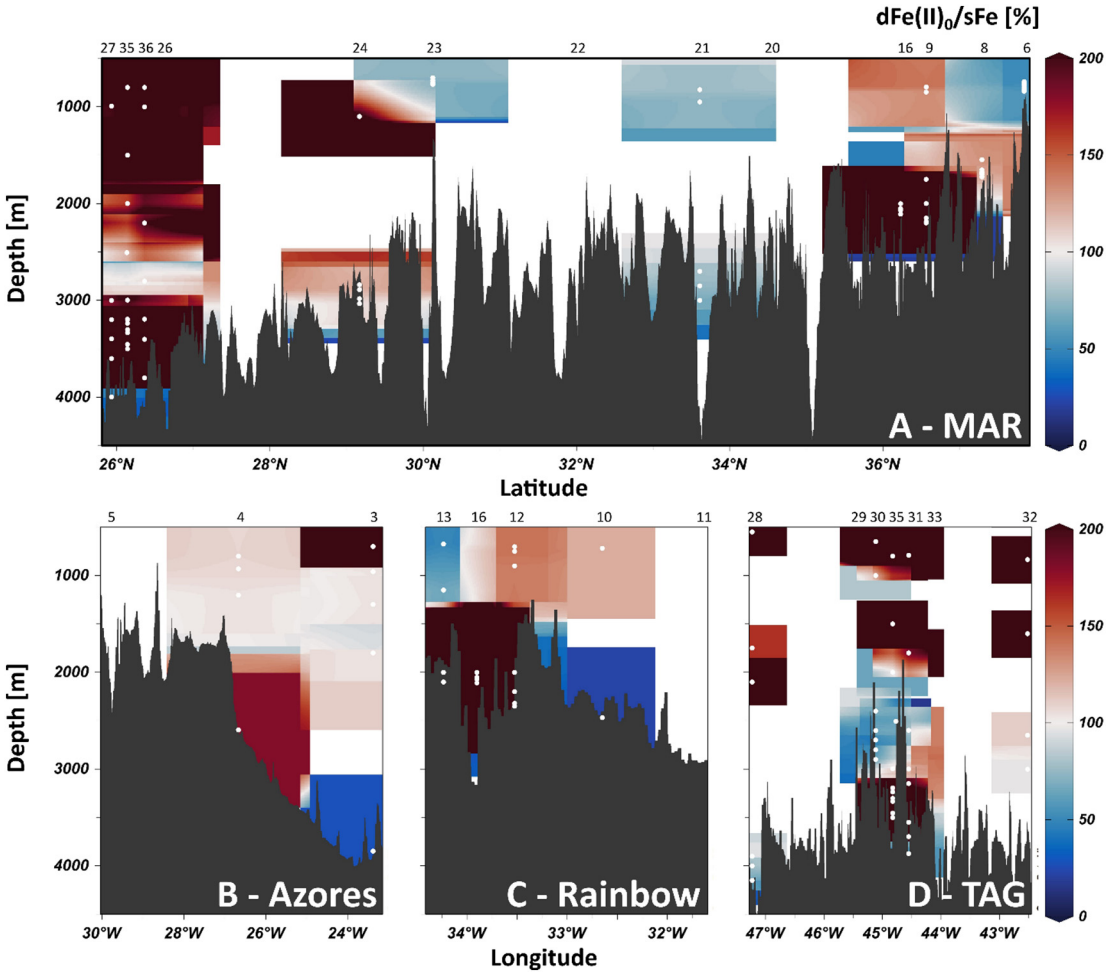

Fig. 7. Vertical sections representing the $dFe(II)_0$ as a fraction of the sFe pool ($dFe(II)_0$/sFe [%]) along the three transects of GEOTRACES cruise GA13 (refer to Fig. 1). Note that the maximum value of the colour scale is 200 %. Top x-axes present the station numbers. In A, stations 35 and 36 were located close to each other, so the label for station 26 has been displaced to the right. In D, stations between 29 and 33 were close to each other so the labels have been positioned relative to their spatial distribution of this data subset.

(2011) who reported percentages of labile Fe(II) as high as 70 % of the dFe pool in waters shallower than 1500 m south of 47°S.

To have a more detailed view of the process, this analysis has been carried out by dividing the water column into its most characteristic layers.

4.1.1. Iron (II) in central waters

One of the main factors affecting Fe(II) oxidation is the O_2 concentration. The OM remineralization process occurs to a greater extent in intermediate waters than in the rest of the water column affecting the dissolved oxygen profile (Supplementary Fig. 2). In this study, the apparent oxygen utilization (AOU) for central waters increased from north to south. The reduction in available oxygen influences Fe(II) oxidation kinetics by decreasing the apparent oxidation rate constant. A significant positive correlation ($r^2 = 0.328$, $n = 306$; p-value $<2 \times 10^{-7}$) was obtained between AOU and dFe(II). Differences in oxygen concentrations between ocean basins can also be attributed to ocean circulation. As such, the more aerated North Atlantic is considered to have a faster Fe(II) oxidation rate than the North Pacific basin (Field and Sherrell, 2000; Statham et al., 2005). This agrees with the results showing that the more O_2 concentrated central waters found north of the transect A presented lower $dFe(II)_0$ concentrations than the southern transects A and D.

The Fe(II) half-life time of a sample with the same temperature, salinity and pH and with dissolved oxygen corresponding to the maximum (250 μmol kg^{-1}) and the minimum (156 μmol kg^{-1}) concentrations in the studied region is 60 % higher under low oxygen conditions (according to Eq. (2)). However, samples with the lowest oxygen concentrations were found at 800-1000 m depth, which presented warmer (7–9.5 °C), higher pH (7.9–8.1) and saltier (35.0–35.5) conditions than deep ocean waters (<5 °C, <7.9, <34, respectively). These variations resulted in a faster Fe (II) oxidation rate within the 800-1000 m deep waters even though the oxygen conditions favoured slower oxidation rates.

Through transects A, B and C, one regional $dFe(II)_0$ maximum is observed at a depth between 1000 and 1500 m. This regional maximum is found above the TAG vent site (St. 35) and presents dFe(II) concentrations averaging 0.22 ± 0.01 nmol L^{-1} ($dFe(II)_0$ = 0.76 ± 0.12 nmol L^{-1}). This regional maximum coincides with the maximum observed by Sedwick et al. (2015) at this specific location. These authors proposed two hypotheses to explain this anomaly. The first hypothesis considered secondary shallow hydrothermal sources located close to TAG. Our oxidation kinetics calculations could not account for the transport of a dFe(II) hydrothermal plume from known shallow sites close to TAG, suggesting that this hypothesis is not probable. The second hypothesis suggested upwelling from the TAG hydrothermal vent site. This work cannot explain how the hydrothermal upwelling could reach 2000 m above the vent site using the Fe(II) results.

4.1.2. Iron (II) in deep waters

In deep waters, the temperature is the factor that plays the largest role in Fe (II) oxidation. At depths >1500 m, in situ temperatures are lower than 5 °C, driving slow oxidation rates of the samples (theoretical $t_{1/2}$ of 53 ± 7 min, n = 377). Measured dFe(II) concentrations were always below

0.1 nmol L^{-1}. However, $dFe(II)_0$ ranged between 0.1 and 0.2 nmol L^{-1}. Consequently, measured dFe(II) concentrations correspond to 28 ± 9 % of what is theoretically calculated considering Fe(II) oxidation rates. These results indicate a possible underestimation of the presence and role of Fe(II) in the deep ocean dFe pool. This underestimation is caused by sampling times, where deep ocean samples are analysed on average two Fe(II) $t_{1/2}$ after being collected.

4.1.3. Iron (II) in hydrothermal areas

The presence of colloidal particles and complexation of the oxidised Fe (II), dominant in the buoyant plume, would affect the rate of Fe(II) oxidation enabling the dissolved Fe(II) to be exported to the non-buoyant plume. The hydrothermal samples were characterised by cFe dominating the dFe pool (90 %). Although Fe-ligand complexes have been studied for the colloidal and soluble pool (Cullen et al., 2006), currently no method exists for the measurement of dissolved Fe(II)-ligand complexes and, similarly, there are no Fe(II) oxidation rate equations considering the organic matter content, type of organic matter, and colloidal particle effects.

The highest measured dFe(II) concentration at the Rainbow site (St. 16; 2108 m depth) was 12.8 nmol L^{-1} ($dFe(II)_0$ = 27.6 nmol L^{-1}) corresponding to 54 % of the dFe ($dFe(II)_0/dFe$ = 116 %). When compared to sFe, dFe (II) was 16 times higher (dFe(II)/sFe = 1615 %; $dFe(II)_0/sFe$ = 3500 %). This discrepancy could be caused by the oxidation of Fe(II) to Fe(III) which forms Fe-oxyhydroxides. Furthermore, colloid aggregation in filters could then influence the dFe partitioning between sFe and cFe during filtration (Massoth et al., 1998). This would explain why <5 % of the dFe was in the soluble size fraction. The dFe(II) and $dFe(II)_0$ profiles (Figs. 4 and 5) display an important behaviour in Fe transport. At stations surrounding the hydrothermal vent sites (30 km from the vents), dFe(II) concentrations had decreased to background levels. Therefore, most of the oxidation of dFe (II) occurred within the first kilometres from the vent sites. This is in agreement with the fast oxidation rate constants reported in these hydrothermal vent sites (González-Santana et al., 2021). High dFe(II) concentrations were also observed at Menez Gwen (0.245 ± 0.012 nmol L^{-1}), Lucky Strike (0.607 ± 0.139 nmol L^{-1}), Broken Spur (0.103 ± 0.010 nmol L^{-1}) and TAG (8.29 ± 1.50 nmol L^{-1}).

4.2. Fe(II) conundrum

In this work, dFe(II) concentrations were above the detection limit throughout the water column far from strong localised sources (e.g. photoreduction, hydrothermal, sediment resuspension, …). Measured dFe(II) concentrations were in agreement with previous work performed in the Atlantic Ocean (Sedwick et al., 2015). Concurrently, due to the seawater physicochemical characteristics, Fe(II) is thermodynamically unstable and oxidises to Fe(III). However, dFe(II) can reach concentrations of up to 0.2 nmol L^{-1} (about 10 times higher than the FIA-CL limit of detection) throughout the water column.

These dFe(II) concentrations could be promoted by the presence of natural organic matter which preserves the Fe(II) by acting as both a redox buffer and a complexant (Daugherty et al., 2017). Reduced natural organic matter could produce a redox buffering mechanism to maintain Fe(II) concentrations which would combine with the reduction of the newly oxidised Fe(III) (Bauer and Kappler, 2009; Daugherty et al., 2017). This process has been observed in laboratory experiments where a low molecular weight quinone (2-methoxyhydroquinone) reduced Fe(III) to Fe(II) faster than the oxidation of Fe(II) due to the presence of oxygen and ROS (Yuan et al., 2016).

These results also led to a scientific conundrum. If dFe(II) concentrations in the deep Atlantic Ocean can be measured in multiple stations and cruises, the Fe(II) sinks and sources in the deep ocean should be approximately equal (we can assume Fe(II) concentrations to be an approximately steady-state). The steady state is maintained by the interaction of biotic loss/sinks and production/sources, abiotic sinks (e.g. oxidation due to the presence of O_2, ROS and H_2O_2) and abiotic sources (e.g. Fe(III)-ligand complexes producing Fe(II) and the oxidised ligand). However, while the samples are in the LDPE bottles, the dFe(II) in the samples is not constant since dFe(II) concentrations decreased (Supplementary Fig. 1). Considering the previous sources and sinks, we can consider the biotic processes to remain within the sample (the sample remains unfiltered). However, within the abiotic processes, the arrival of fresh ligands capable of complexing Fe(III) and Fe(II) is blocked, limiting an abiotic source and stabilisation of dFe(II). These processes should occur within the OTE bottles which collected the sample from the deep ocean. Oxidation kinetics experiments have been performed maintaining the sample within Niskin bottles (Statham et al., 2005). Unfortunately, we currently do not have the technology for the in-situ detection of Fe(II) concentrations with picomolar detection limits nor the knowledge of how to quickly stabilize the dFe(II) in the water without affecting the redox speciation of Fe. Future studies should emulate our approach, carefully monitoring times between sampling and analysis and checking Fe(II) loss within the LDPE bottle and OTE bottles to thoroughly verify if dFe(II) is lost within the sampling bottles or if Fe (II) concentrations are maintained due to processes and reactions occurring within them. This would allow for more robust comparisons between studies, which is key to understanding the role of redox processes governing the Fe cycle.

5. Conclusions

The GA13 cruise has provided new data on the North MAR. Measured dFe(II) concentrations throughout the water column were low, with concentrations below 0.2 nmol L^{-1}, decreasing in the deep ocean to <0.1 nmol L^{-1}. In our study, we have identified some sources and physicochemical conditions which modulate the dFe(II) profile. Over the whole water column, the oxidation of Fe(II) is a limiting factor, with measured dFe(II) concentrations only accounting for 10 to 65 % of the computed original Fe(II) concentrations. The factors involved in the oxidation vary by ocean depths.

In the surface waters, the photoreduction of Fe(III) forms Fe(II). Nevertheless, physicochemical parameters as high seawater temperature above 15 °C, high pH and highly oxic waters influence the Fe(II) half-life in the surface layer, shortening the $t_{1/2}$ to 3 to 100 times shorter than the time required to analyse the samples. Concurrently, biological activities excrete organic matter affecting the Fe(II) concentrations and its residence time. Even so, computed original Fe(II) concentrations are difficult to determine if the $t_{1/2}$ are too short.

In the central waters, where the minimum oxygen zone is produced as a result of organic matter remineralisation, the conditions allow for a slower oxidation rate, where measured dFe(II) concentrations increase. Oxygen variations within this section accounted for a Fe(II) half-life variation of up to 60 %. Finally, in the deep ocean, hydrothermal activity acts as a source of Fe(II), whose concentrations will depend on the vent site, the distance from the vent to the sampling point and the oxidation rate. Furthermore, in all cases, the Fe(II) oxidation rate constant is also dependent on the presence of organic matter and colloidal size particles, but these two variables have not been considered here, since the oxidation rate equation only accounts for some inorganic processes. Organic matter is a pool of thousands of individual compounds each of them with varying impacts on oxidation rates. We consider that these two factors should not be major sources of uncertainty in the determination of $dFe(II)_0$ within this study. The OM and colloidal effect should be implicitly accounted for in the oxidation rate constant equation since it was developed with samples collected in the same cruise at the same depths. Moreover, the OM effect was more significant in shallow (<500 m) samples (González-Santana et al., 2021), which have not been included in this manuscript.

This work has shown that $dFe(II)_0$ could account for >20 % of the dFe pool and not only <10 % as previously reported (Boye et al., 2006; Sarthou et al., 2011; Sedwick et al., 2015) when the oxidation during sampling and analysis time is taken into account. The importance of Fe(II) oxidation is not only related to Fe(II) concentrations and their proportions to the Fe pool but the effect on the quantification of other Fe cycle parameters. The fast oxidation rate of Fe(II) makes Fe speciation difficult to establish,

and its oxidation can influence its size fractionation. As such, a portion of the mainly soluble sized Fe(II) will oxidize to the colloidal size fraction or get adsorbed onto larger particles. Oxidation of Fe(II) will affect more common measurements such as sFe, cFe and dFe. Therefore, future studies observing Fe concentrations should check for Fe losses during the sampling processes by taking additional Fe samples at the middle and end of the sampling process and recording sampling and analysis times. This is of particular importance in environments likely to have elevated Fe(II) concentrations such as hydrothermal plumes, oxygen minimum zones, meltwater from sub-glacial streams and release of Fe from sub/anoxic sediments.

Author contributions

DG-S analysed the dFe(II) and pH samples. AJML analysed the sFe and dFe samples. ML was in charge of the trace metal sampling team. DG-S, HP and GS wrote the manuscript with significant contributions from all co-authors. All the authors contributed to the article and approved the submitted version.

Funding

Work was supported by NERC (NE/N010396/1 and NE/N009525/1) awards to AT and MCL.

Data availability

I have added all the data (including calculated data) as a supplementary file.

Declaration of competing interest

The authors declare that they have no known competing financial interests or personal relationships that could have appeared to influence the work reported in this paper.

Acknowledgements

The authors would like to thank the captain and crew of the *R.R.S. James Cook* as well as the scientific team during the GA13 cruise. The International GEOTRACES Programme is possible in part thanks to the support from the U.S. National Science Foundation (Grant OCE-1840868) to the Scientific Committee on Oceanic Research (SCOR).

Appendix A. Supplementary data

Supplementary data to this article can be found online at https://doi.org/10.1016/j.scitotenv.2022.161179.

References

Ardyna, M., Lacour, L., Sergi, S., D'Ovidio, F., Sallée, J.-B., Rembauville, M., Blain, S., Tagliabue, A., Schlitzer, R., Jeandel, C., 2019. Hydrothermal vents trigger massive phytoplankton blooms in the Southern Ocean. Nat. Commun. 10, 1–8. https://doi.org/10.1038/s41467-019-09973-6.

Bauer, I., Kappler, A., 2009. Rates and extent of reduction of Fe(III) compounds and O2 by humic substances. Environ. Sci. Technol. 43, 4902–4908. https://doi.org/10.1021/es900179s.

Bennett, S.A., Achterberg, E.P., Connelly, D.P., Statham, P.J., Fones, G.R., German, C.R., 2008. The distribution and stabilisation of dissolved Fe in deep-sea hydrothermal plumes. Earth Planet. Sci. Lett. 270, 157–167. https://doi.org/10.1016/j.epsl.2008.01.048.

Bowie, A.R., Achterberg, E.P., Sedwick, P.N., Ussher, S.J., Worsfold, P.J., 2002. Real-time monitoring of picomolar concentrations of Iron(II) in marine waters using automated flow injection-chemiluminescence instrumentation. Environ. Sci. Technol. 36, 4600–4607. https://doi.org/10.1021/es020045v.

Bowie, A.R., Sedwick, P.N., Worsfold, P.J., 2004. Analytical intercomparison between flow injection-chemiluminescence and flow injection-spectrophotometry for the determination of picomolar concentrations of iron in seawater. Limnol. Oceanogr. Methods 2, 42–54. https://doi.org/10.4319/lom.2004.2.42.

Boyd, P.W., Ibisanmi, E., Sander, S.G., Hunter, K.A., Jackson, G.A., 2010. Remineralization of upper ocean particles: implications for iron biogeochemistry. Limnol. Oceanogr. 55, 1271–1288. https://doi.org/10.4319/lo.2010.55.3.1271.

Boye, M., Aldrich, A., van den Berg, C.M.G., de Jong, J.T.M., Nirmaier, H., Veldhuis, M.J.W., Timmermans, K.R., de Baar, H.J.W., 2006. The chemical speciation of iron in the northeast Atlantic Ocean. DeepRes. Part I Oceanogr. Res. Pap. 53, 667–683. https://doi.org/10.1016/j.dsr.2005.12.015.

Canfield, D.E., Stewart, F.J., Thamdrup, B., De Brabandere, L., Dalsgaard, T., DeLong, E.F., Revsbech, N.P., Ulloa, O., 2010. A cryptic sulfur cycle in oxygen-minimum-zone waters off the Chilean coast. Science 330, 1375–1378. https://doi.org/10.1126/science.1196889.

Cullen, J.T., Bergquist, B.A., Moffett, J.W., 2006. Thermodynamic characterization of the partitioning of iron between soluble and colloidal species in the Atlantic Ocean. Mar. Chem. 98, 295–303. https://doi.org/10.1016/J.MARCHEM.2005.10.007.

Daugherty, E.E., Gilbert, B., Nico, P.S., Borch, T., 2017. Complexation and redox buffering of Iron(II) by dissolved organic matter. Environ. Sci. Technol. 51, 11096–11104. https://doi.org/10.1021/acs.est.7b03152.

Edwards, K.J., Glazer, B.T., Rouxel, O.J., Bach, W., Emerson, D., Davis, R.E., Toner, B.M., Chan, C.S., Tebo, B.M., Staudigel, H., Moyer, C.L., 2011. Ultra-diffuse hydrothermal venting supports Fe-oxidizing bacteria and massive umber deposition at 5000 m off Hawaii. ISME J. 5, 1748–1758. https://doi.org/10.1038/ismej.2011.48 2011 511.

Emerson, D., Rentz, J., Lilburn, T., Davis, R., Aldrich, H., 2007. A novel lineage of proteobacteria involved in formation of marine Fe-oxidizing microbial mat communities. PLoS One 8.

Field, M.P., Sherrell, R.M., 2000. Dissolved and particulate Fe in a hydrothermal plume at 9°45'N, East Pacific rise: slow Fe (II) oxidation kinetics in Pacific plumes. Geochim. Cosmochim. Acta 64, 619–628. https://doi.org/10.1016/S0016-7037(99)00333-6.

Findlay, A.J., Estes, E.R., Gartman, A., Yücel, M., Kamyshny, A., Luther III, G.W., 2019. Iron and sulfide nanoparticle formation and transport in nascent hydrothermal vent plumes. Nat. Commun. 10, 1–7.

Fitzsimmons, J.N., Carrasco, G.G., Wu, J., Roshan, S., Hatta, M., Conway, T.J., John, S.G., Boyle, E.A., 2015. Partitioning of dissolved iron and iron isotopes into soluble and colloidal phases along the GA03 GEOTRACES North Atlantic Transect. Deep Sea Res.Part II Top. Stud. Oceanogr. 116, 130–151.

Fitzsimmons, J.N., John, S.G., Marsay, C.M., Hoffman, C.L., Nicholas, S.L., Toner, B.M., German, C.R., Sherrell, R.M., 2017. Iron persistence in a distal hydrothermal plume supported by dissolved-particulate exchange. Nat. Geosci. 10, 195–201. https://doi.org/10.1038/ngeo2900.

Fouquet, Y., Cambon, P., Etoubleau, J., Charlou, J.L., Ondréas, H., Barriga, F.J.A.S., Cherkashov, G., Semkova, T., Poroshina, I., Bohn, M., Donval, J.-P., Henry, K., Murphy, P., Rouxel, O., 2013. Geodiversity of hydrothermal processes along the Mid-Atlantic Ridge and ultramafic-hosted mineralization: a new type of oceanic Cu-Zn-Co-Au volcanogenic massive sulfide deposit. Diversity of Hydrothermal Systems on Slow Spreading Ocean Ridges Diversity of Hydrothermal Systems on Slow Spreading Ocean Ridges. Wiley-Blackwell, pp. 321–367 https://doi.org/10.1029/2008GM000746.

González-Santana, D., Planquette, H., Cheize, M., Whitby, H., Gourain, A., Holmes, T.M., Guyader, V., Cathalot, C., Pelleter, E., Fouquet, Y., Sarthou, G., 2020. Processes driving iron and manganese dispersal from the TAG hydrothermal plume (Mid-Atlantic Ridge): results from a GEOTRACES process study. Front. Mar. Sci. 7, 568. https://doi.org/10.3389/fmars.2020.00568.

González-Santana, D., González-Dávila, M., Lohan, M.C., Artigue, L., Planquette, H., Sarthou, G., Tagliabue, A., Santana-Casiano, J.M., 2021. Variability in iron (II) oxidation kinetics across diverse hydrothermal sites on the northern Mid Atlantic Ridge. Geochim. Cosmochim. Acta 297, 143–157. https://doi.org/10.1016/j.gca.2021.01.013.

Guieu, C., Bonnet, S., Petrenko, A., Menkes, C., Chavagnac, V., Desboeufs, K., Maes, C., Moutin, T., Chavagnac, V., Petrenko, A., Bonnet, S., Guieu, C., Menkes, C., Maes, C., 2018. Iron from a submarine source impacts the productive layer of the Western Tropical South Pacific (WTSP). Sci. Rep. 8, 9075. https://doi.org/10.1038/s41598-018-27407-z.

Hansard, S.P., Landing, W.M., Measures, C.I., Voelker, B.M., 2009. Dissolved iron(II) in the Pacific Ocean: measurements from the PO2 and P16N CLIVAR/CO2 repeat hydrography expeditions. Deep Sea Res.Part I Oceanogr. Res. Pap. 56, 1117–1129. https://doi.org/10.1016/J.DSR.2009.03.006.

Hawkes, J.A., Connelly, D.P., Gledhill, M., Achterberg, E.P., 2013. The stabilisation and transportation of dissolved iron from high temperature hydrothermal vent systems. Earth Planet. Sci. Lett. 375, 280–290.

Humphris, S.E., Tivey, M.K., Tivey, M.A., 2015. The Trans-Atlantic Geotraverse hydrothermal field: a hydrothermal system on an active detachment fault. Deep Res. Part II Top. Stud. Oceanogr. https://doi.org/10.1016/j.dsr2.2015.02.015.

Klar, J.K., Homoky, W.B., Statham, P.J., Birchill, A.J., Harris, E.L., Woodward, E.M.S., Silburn, B., Cooper, M.J., James, R.H., Connelly, D.P., Chever, F., Lichtschlag, A., Graves, C., 2017. Stability of dissolved and soluble Fe(II) in shelf sediment pore waters and release to an oxic water column. Biogeochemistry 135, 49–67. https://doi.org/10.1007/s10533-017-0309-x.

Klinkhammer, G.P., Chin, C.S., Keller, R.A., Dählmann, A., Sahling, H., Sarthou, G., Petersen, S., Smith, F., Wilson, C., 2001. Discovery of new hydrothermal vent sites in Bransfield Strait,Antarctica. Earth Planet. Sci. Lett. 193, 395–407. https://doi.org/10.1016/S0012-821X(01)00536-2.

Klueglein, N., Zeitvogel, F., Stierhof, Y.D., Floetenmeyer, M., Konhauser, K.O., Kappler, A., Obst, M., 2014. Potential role of nitrite for abiotic Fe(II) oxidation and cell encrustation during nitrate reduction by denitrifying bacteria. Appl. Environ. Microbiol. 80, 1051–1061. https://doi.org/10.1128/AEM.03277-13.

Liu, X., Millero, F.J., 2002. The solubility of iron in seawater. Mar. Chem. 77, 43–54. https://doi.org/10.1016/S0304-4203(01)00074-3.

Lohan, M.C., Aguilar-Islas, A.M., Bruland, K.W., 2006. Direct determination of iron in acidified (pH 1.7) seawater samples by flow injection analysis with catalytic spectrophotometric detection: application and intercomparison. Limnol. Oceanogr. Methods 4, 164–171. https://doi.org/10.4319/lom.2006.4.164.

Lough, A.J.M., Klar, J.K., Homoky, W.B., Comer-Warner, S.A., Milton, J.A., Connelly, D.P., James, R.H., Mills, R.A., 2017. Opposing authigenic controls on the isotopic signature of dissolved iron in hydrothermal plumes. Geochim. Cosmochim. Acta 202, 1–20. https://doi.org/10.1016/j.gca.2016.12.022.

Lough, A.J.M., Homoky, W.B., Connelly, D.P., Comer-Warner, S.A., Nakamura, K., Abyaneh, M.K., Kaulich, B., Mills, R.A., 2019. Soluble iron conservation and colloidal iron dynamics in a hydrothermal plume. Chem. Geol. 511, 225–237.

Lueker, T.J., Dickson, A.G., Keeling, C.D., 2000. Ocean pCO2 calculated from dissolved inorganic carbon, alkalinity, and equations for K1 and K2: validation based on laboratory measurements of CO2 in gas and seawater at equilibrium. Mar. Chem. 70, 105–119. https://doi.org/10.1016/S0304-4203(00)00022-0.

Lyons, T.W., Reinhard, C.T., Planavsky, N.J., 2014. The rise of oxygen in Earth's early ocean and atmosphere. Nature 506, 307–315. https://doi.org/10.1038/nature13068.

Maldonado, M.T., Price, N.M., 1999. Utilization of Iron Bound to Strong Organic Ligands by Plankton Communities in the Subarctic Pacific Ocean. 46, pp. 2447–2473. https://doi.org/10.1016/S0967-0645(99)00071-5.

Maldonado, M.T., Price, N.M., 2000. Nitrate regulation of Fe reduction and transport by Fe-limited Thalassiosira oceanica. Limnol. Oceanogr. 45, 814–826. https://doi.org/10.4319/lo.2000.45.4.0814.

Maldonado, M.T., Price, N.M., 2001. Reduction and transport of organically bound iron by Thalassiosira oceanica (Bacillariophyceae). J. Phycol. 37, 298–310.

Massoth, G.J., Baker, E.T., Feely, R.A., Lupton, J.E., Collier, R.W., Gendron, J.F., Roe, K.K., Maenner, S.M., Resing, J.A., 1998. Manganese and iron in hydrothermal plumes resulting from the 1996 Gorda Ridge Event. Deep Sea Res.Part II Top. Stud. Oceanogr. 45, 2683–2712.

Millero, F.J., 1986. The pH of estuarine waters. Limnol. Oceanogr. 31, 839–847. https://doi.org/10.4319/lo.1986.31.4.0839.

Millero, F.J., Sotolongo, S., Izaguirre, M., 1987. The oxidation kinetics of Fe(II) in seawater. Geochim. Cosmochim. Acta 51, 793–801. https://doi.org/10.1016/0016-7037(87)90093-7.

Millero, F.J., Yao, W., Aicher, J., 1995. The speciation of Fe (II) and Fe (III) in natural waters. Mar. Chem. 50, 21–39.

Moffett, J.W., 2021. Iron(II) in the world's oxygen deficient zones. Chem. Geol. 120314. https://doi.org/10.1016/j.chemgeo.2021.120314.

Morel, F.M., Hering, J., 1993. Principles and Applications of Aquatic Chemistry. Wiley-Interscience.

Nishioka, J., Obata, H., Tsumune, D., 2013. Evidence of an extensive spread of hydrothermal dissolved iron in the Indian Ocean. Earth Planet. Sci. Lett. 361, 26–33.

Obata, H., Karatani, H., Nakayama, E., 1993. Automated determination of iron in seawater by chelating resin concentration and chemiluminescence detection. Anal. Chem. 65, 1524–1528. https://doi.org/10.1021/ac00059a007.

O'Sullivan, D.W., Hanson, A.K., Miller, W.L., Kester, D.R., 1991. Measurement of Fe (II) in surface water of the equatorial Pacific. Limnol. Oceanogr. 36, 1727–1741.

Raven, J.A., Evans, M.C.W., Korb, R.E., 1999. The role of trace metals in photosynthetic electron transport in O-2-evolving organisms. Photosynth. Res. 60, 111–149. https://doi.org/10.1023/a:1006282714942.

Resing, J.A., Sedwick, P.N., German, C.R., Jenkins, W.J., Moffett, J.W., Sohst, B.M., Tagliabue, A., 2015. Basin-scale transport of hydrothermal dissolved metals across the South Pacific Ocean. Nature 523, 200–203. https://doi.org/10.1038/nature14577.

Rose, A.L., 2012. The influence of extracellular superoxide on iron redox chemistry and bioavailability to aquatic microorganisms. Front. Microbiol. https://doi.org/10.3389/fmicb.2012.00124.

Roshan, S., DeVries, T., Wu, J., John, S.G., Weber, T., 2020. Reversible scavenging traps hydrothermal iron in the deep ocean. Earth Planet. Sci. Lett. 542, 116297. https://doi.org/10.1016/J.EPSL.2020.116297.

Roy, E.G., Wells, M.L., 2011. Evidence for regulation of Fe (II) oxidation by organic complexing ligands in the Eastern Subarctic Pacific. Mar. Chem. 127, 115–122.

Roy, E.G., Wells, M.L., King, D.W., 2008. Persistence of iron (II) in surface waters of the western subarctic Pacific. Limnol. Oceanogr. 53, 89–98.

Rudnicki, M.D., Elderfield, H., 1993. A chemical model of the buoyant and neutrally buoyant plume above the TAG vent field, 26 degrees N,Mid-Atlantic Ridge. Geochim. Cosmochim. Acta 57, 2939–2957. https://doi.org/10.1016/0016-7037(93)90285-5.

Rue, E.L., Bruland, K.W., 1997. The role of organic complexation on ambient iron chemistry in the equatorial Pacific Ocean and the response of a mesoscale iron addition experiment. Limnol. Oceanogr. 42, 901–910.

Santana-Casiano, J.M., González-Dávila, M., Rodríguez, M.J., Millero, F.J., 2000. The effect of organic compounds in the oxidation kinetics of Fe(II). Mar. Chem. 70, 211–222. https://doi.org/10.1016/S0304-4203(00)00027-X.

Santana-Casiano, J.M., González-Dávila, M., Millero, F.J., 2005. Oxidation of nanomolar level of Fe(II) with oxygen in natural waters. Environ. Sci. Technol. 39, 2073–2079. https://doi.org/10.1021/es049748y.

Santana-Casiano, J.M., González-Dávila, M., Millero, F.J., 2006. The role of Fe(II) species on the oxidation of Fe(II) in natural waters in the presence of O2 and H2O2. Mar. Chem. 99, 70–82. https://doi.org/10.1016/j.marchem.2005.03.010.

Santana-González, C., González-Dávila, M., Santana-Casiano, J.M., Gladyshev, S., Sokov, A., 2019. Organic matter effect on Fe(II) oxidation kinetics in the Labrador Sea. Chem. Geol. 511, 238–255. https://doi.org/10.1016/j.chemgeo.2018.12.019.

Sarthou, G., Bucciarelli, E., Chever, F., Hansard, S.P., González-Dávila, M., Santana-Casiano, J.M., Planchon, F., Speich, S., 2011. Labile Fe(II) concentrations in the Atlantic sector of the Southern Ocean along a transect from the subtropical domain to the Weddell Sea Gyre. Biogeosciences 8, 2461–2479. https://doi.org/10.5194/bg-8-2461-2011.

Schallenberg, C., Davidson, A.B., Simpson, K.G., Miller, L.A., Cullen, J.T., 2015. Iron (II) variability in the northeast subarctic Pacific Ocean. Mar. Chem. 177, 33–44.

Schine, C.M.S., Alderkamp, A.-C., van Dijken, G., Gerringa, L.J.A., Sergi, S., Laan, P., van Haren, H., van de Poll, W.H., Arrigo, K.R., 2021. Massive Southern Ocean phytoplankton bloom fed by iron of possible hydrothermal origin. Nat. Commun. 12, 1–11. https://doi.org/10.1038/s41467-021-21339-5 2021 121.

Sedwick, P.N., Sohst, B.M., Ussher, S.J., Bowie, A.R., 2015. A zonal picture of the water column distribution of dissolved iron(II) during the U.S. GEOTRACES North Atlantic transect cruise (GEOTRACES GA03). DeepRes. Part II Top. Stud. Oceanogr. 116, 166–175. https://doi.org/10.1016/j.dsr2.2014.11.004.

Sieber, M., Conway, T.M., de Souza, G.F., Hassler, C.S., Ellwood, M.J., Vance, D., 2021. Isotopic fingerprinting of biogeochemical processes and iron sources in the iron-limited surface Southern Ocean. Earth Planet. Sci. Lett. 567, 116967. https://doi.org/10.1016/J.EPSL.2021.116967.

Singer, E., Emerson, D., Webb, E.A., Barco, R.A., Kuenen, J.G., Nelson, W.C., Chan, C.S., Comolli, L.R., Ferriera, S., Johnson, J., Heidelberg, J.F., Edwards, K.J., 2011. Mariprofundus ferrooxydans PV-1 the first genome of a marine Fe(II) oxidizing zetaproteobacterium. PLoS One 6, e25386. https://doi.org/10.1371/journal.pone.0025386.

Statham, P.J., German, C.R., Connelly, D.P., 2005. Iron (II) distribution and oxidation kinetics in hydrothermal plumes at the Kairei and Edmond vent sites,Indian Ocean. Earth Planet. Sci. Lett. 236, 588–596. https://doi.org/10.1016/J.EPSL.2005.03.008.

Straub, K.L., Benz, M., Schink, B., 2001. Iron metabolism in anoxic environments at near neutral pH. FEMS Microbiol. Ecol. 34, 181–186.

Straub, K.L., Schönhuber, W.A., Buchholz-Cleven, B.E.E., Schink, B., 2004. Diversity of ferrous iron-oxidizing, nitrate-reducing bacteria and their involvement in oxygen-independent iron cycling. Geomicrobiol. J. 21, 371–378.

Tagliabue, A., Resing, J.A., 2016. Impact of hydrothermalism on the ocean iron cycle. Philos. Trans. R. Soc. A Math. Phys. Eng. Sci. 374. https://doi.org/10.1098/rsta.2015.0291.

Tagliabue, A., Bopp, L., Dutay, J.C., Bowie, A.R., Chever, F., Jean-Baptiste, P., Bucciarelli, E., Lannuzel, D., Remenyi, T., Sarthou, G., Aumont, O., Gehlen, M., Jeandel, C., 2010. Hydrothermal contribution to the oceanic dissolved iron inventory. Nat. Geosci. 3, 252–256. https://doi.org/10.1038/ngeo818.

Theis, T.L., Singer, P.C., 1974. Complexation of iron (II) by organic matter and its effect on iron (II) oxygenation. Environ. Sci. Technol. 8, 569–573.

Ussher, S.J., Achterberg, E.P., Sarthou, G., Laan, P., de Baar, H.J.W., Worsfold, P.J., 2010. Distribution of size fractionated dissolved iron in the Canary Basin. Mar. Environ. Res. 70, 46–55. https://doi.org/10.1016/j.marenvres.2010.03.001.

Vedamati, J., Goepfert, T.J., Moffett, J.W., 2014. Iron speciation in the eastern tropical South Pacific oxygen minimum zone off Peru. Limnol. Oceanogr. 59, 1945–1957. https://doi.org/10.4319/lo.2014.59.6.1945.

Voelker, B.M., Morel, F.M., Sulzberger, B., 1997. Iron Redox Cycling in Surface Waters: Effects of Humic Substances and Light. 31, pp. 1004–1011. https://doi.org/10.1021/es9604018.

Yao, W., Millero, F.J., 1996. Oxidation of hydrogen sulfide by hydrous Fe(III) oxides in seawater. Mar. Chem. 52, 1–16. https://doi.org/10.1016/0304-4203(95)00072-0.

Yuan, X., Davis, J.A., Nico, P.S., 2016. Iron-mediated oxidation of methoxyhydroquinone under dark conditions: kinetic and mechanistic insights. Environ. Sci. Technol. 50, 1731–1740. https://doi.org/10.1021/acs.est.5b03939.